

# Segmenting the external surface of a human skull in MRI data by adding shape information to gradient vector flow snakes

Miguel Salas, Steve Maddock  
Department of Computer Science, University of Sheffield  
211 Portobello Street, Sheffield, S1 4DP, UK  
{M.Salas,S.Maddock}@dcs.shef.ac.uk

September 17, 2007

## Abstract

This paper presents a method for segmenting bone in magnetic resonance images. The starting point is the formulation of a Gradient Vector Flow (GVF) snake extended to include statistical shape information. This method exploits the diffusion process used by the GVF snake and improves its capacity to deal with occlusion problems by adding a shape term to the traditional scheme. A dataset of coronal MR images of the Visible Human Project is used to extract an outline of the skull region. The results of the segmentation are compared with a segmentation of bone areas taken from CT scans of the same individual. For the MR data, the addition of a shape term improves on the results obtained by using a GVF snake alone.

**Index Terms:** parametric snakes, active contours, shape analysis, skull segmentation.

## 1 Introduction

In the area of forensic cranio-facial reconstruction, a key element to produce reliable facial estimations is the knowledge of the relation between the facial soft tissue and the underlying skull. All the current craniofacial reconstruction systems (i.e. manual and computer-assisted) are based on this knowledge [16]. Due to the complexity of the facial configuration, this relationship is currently known only at a discrete set of points on the skull and face. These points are known as anthropometric landmarks. This data is usually collected by hand and from individuals of a specific ethnic group. In

this work, we investigate the possibility of using 3D cross-sectional magnetic resonance (MR) images for establishing a reference database where the skull and face surfaces can be studied in a more extensive manner. The skull surface will be extracted by bi-dimensionally segmenting a set of images of an MR volume. The extracted contours will be used to create a 3D skull model. Figure 1 shows the multiple slice structure of an MR dataset. The

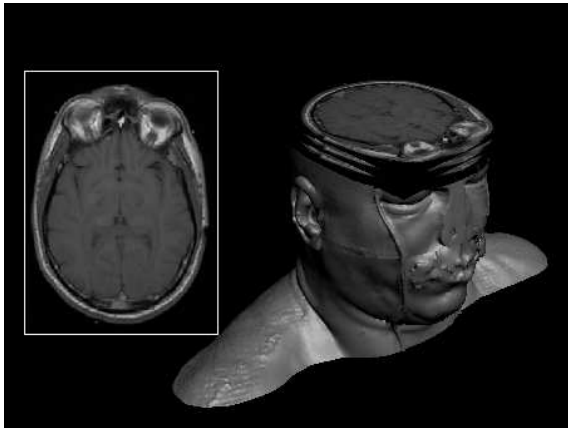


Figure 1: The magnetic resonance male dataset from the VHP project [2, 13, 14]. Left: a typical MR scan image. Right: the structure of the volume.

segmentation process we propose is made up of two components. The first component is an active contour directed by image features which ‘blindly’ tries to enclose skull areas. The second component is a shape term which adds statistical knowledge of the

likely shape to find. Specifically, for this work, a gradient vector flow (GVF) snake approach is extended to include the shape term proposed by Cremers et al. [6, 7]. This shape term was originally designed to be used with a Mumford-Shah functional and a dynamic potential force. In our approach, these two components are used to make an active contour to evolve towards a minimum within the static potential field calculated from the gradient information. Our algorithm differs from Cremers et al.’s version in the type of potential force used for controlling the snake evolution. Cremers et al. use a dynamic criteria for calculating the potential depending on the snake neighborhood and the image homogeneity, whilst we use a static potential force based on the gradient information.

For this work, we will use the Magnetic Resonance (MR) 3D dataset of the male head from the Visible Human Project [2, 13, 14]. A Computer Tomography (CT) volume of the same person is also available and will be used to validate the results. Figure 2 shows an example of these two modalities for a given region.

Segmenting the skull in a CT image is relatively easy because bone areas are well defined in this scan modality. However, its use is limited because of the involved radiation dose [16]. In contrast, MRI is a safer option for scanning live individuals. Nevertheless, in this modality the chemical composition of the bone presents low response to magnetic stimulus. This property causes bone areas to be partially defined in some portions of the image, and mixed with distinct tissues and air in others, which makes the skull segmentation difficult. This is the problem our approach attempts to solve. To assess the performance of our proposed algorithm, the results of the MR segmentation will be compared with the results of segmenting the same bone area in a CT image.

Section 2 provides an overview of the general active contour terminology. In Section 3, the gradient vector flow (GVF) snake and its potential field is introduced. Section 4 describes the inclusion of statistical shape knowledge to the active contour formulation. Section 5 presents the experimental results and, finally, in section 6 the conclusions are presented.

## 2 Active Contours

Active contours (or snakes)<sup>1</sup> are widely used for boundary detection in the field of image segmentation and computer vision [1, 10]. The classical approach is based on deforming an initial contour  $C_o$  towards the boundary of the object to be detected, making this contour converge to an optimal final state (i.e. a curve at the contour of the desired object) from an arbitrary initial state (i.e. shape and position). The deformation is obtained by minimizing a functional designed so that its minimum is obtained at the boundary of the object [5]. The functional consists of two main components. One component controls the smoothness of the curve and the other attracts the curve toward the image features. These two components are known as the internal and external forces, respectively [15, 11].

Two types of active contour models are common in the literature: parametric active contours [11] and geometric contours [4, 12]. In our work we use an extension to a parametric active contour, defined as a parametric curve moving toward desired features (edges) under the influence of potential forces. A potential force is a bi-dimensional function assigning to all the pixels in the image domain a magnitude and a direction of influence. In our work, this function is derived from the image gradient and accounts for the influence of the image data on the snake.

In general, the problems which must be overcome with the application of active contours are:

- Initialization: The range of capture of traditional potential forces is small. The range of capture is the area around an image feature where a force potential is defined to attract the active contour (see figure 3).
- Concave regions: Difficulties can occur when progressing the curve into concave boundary regions.
- Occlusion Problems: Sometimes it is necessary to deal with missing information in the image.

A traditional formulation for a snake is a curve  $x(s) = [x(s), y(s)]$ ,  $s \in [0, 1]$  that moves through

---

<sup>1</sup>The terms active contour and snake will be used interchangeably in this document.

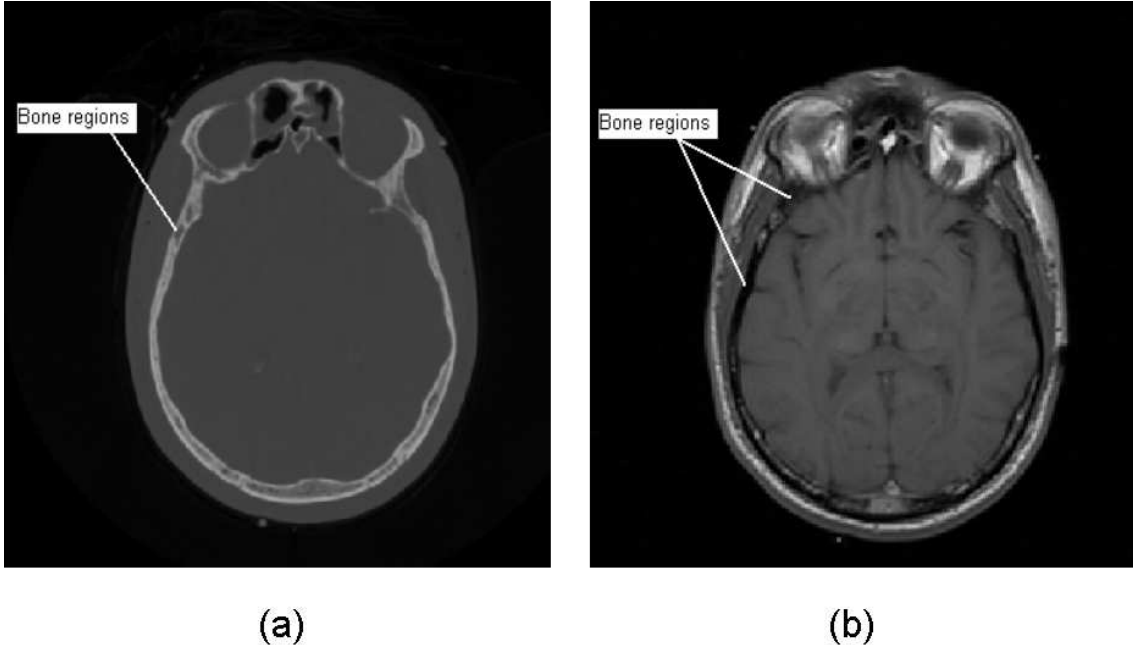


Figure 2: A slice of a human head (from the VHP dataset) showing the same anatomical region, approximately at the level of the eyes with a view from above the head. (a) The CT scan version and (b) the MR version.

the spatial domain  $\Omega$  of an image in order to minimize the following functional [5]:

$$E_t = \int_0^1 \left( \frac{1}{2} (\alpha |x'(s)|^2 + \beta |x''(s)|^2 + E_{ext}(x(s))) \right) ds \quad (1)$$

where  $x'(s)$  and  $x''(s)$  stand for the first and second derivative of the curve  $x$  with respect to  $s$ , and  $\alpha$  and  $\beta$  are weighting parameters that control the active contour tension and rigidity [11]. The external energy  $E_{ext}$  is obtained from the image and reaches its lower values at interest features such as boundaries. The next section introduces the particular kind of active contour we use.

### 3 Gradient vector flow active contours

Gradient vector flow (GVF) active contours are curves under the influence of a potential force called gradient vector flow [18]. The gradient vector flow

is an external force computed as a diffusion of the gradient vectors of the image. This force is used to attract the snake towards the edges in the image. The evolution of a GVF snake can be formulated by solving equation (1). This solution can be obtained by minimizing the following Euler equation:

$$\alpha x''(s) + \beta x''''(s) - \nabla E_{ext} = 0 \quad (2)$$

which is equivalent to the following system of forces:

$$F_{int} + F_{ext} = 0 \quad (3)$$

with  $F_{int} = \alpha x''(s) + \beta x''''(s)$  and  $F_{ext} = -\nabla E_{ext}$

The term  $F_{int}$  accounts for the geometric restrictions of the snake itself (tension and rigidity) and the second term  $F_{ext}$  accounts for the evolution towards image features. The external forces  $F_{ext}$  can be divided into two classes: static and dynamic [17]. Static forces are computed from the image data and do not change as the snake progresses. Dynamic forces are those that change as the snake deforms. We use a static GVF force, which is a type of static

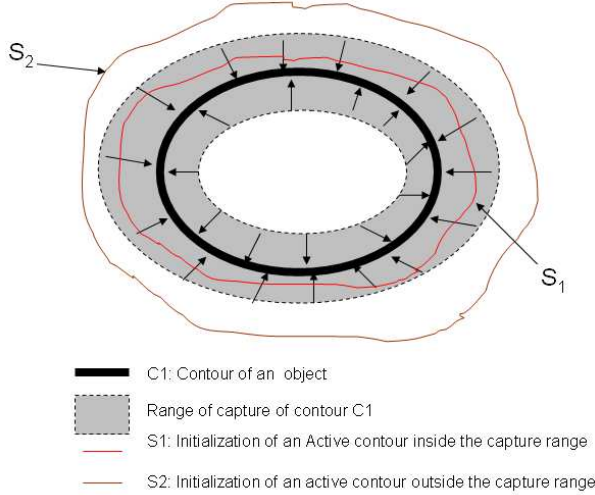


Figure 3: Capture range of an elliptic object. In this example the contour  $S_1$  is under the influence of the border of the ellipse  $C_1$  while  $S_2$  is not. In this case, the contour  $S_2$  will not be deformed.

external force independent of the time and the position of the snake.

To find a solution to equation (2) the snake is made dynamic by treating  $x$  as a function of time  $t$  as well as the spline parameter  $s$ . i.e.  $x(s, t)$ . Then a partial derivative of  $x$  with respect to  $t$  is set equal to the left side of equation (2) as follows:

$$x_t(s, t) = \alpha x''(s, t) + \beta x''''(s, t) - \nabla E_{ext} \quad (4)$$

When the solution  $x(s, t)$  stabilizes, the term  $x_t(s, t)$  gradually disappears and we achieve a solution for equation (2).

To complete the definition of a GVF active contour it is necessary to define the potential force influencing the curve evolution. This potential force is called the gradient vector flow and it is defined over an edge map of the image. This concept will be introduced in the next subsections.

### 3.1 Edge Maps and GVF field formulation

To define potential external forces acting on the active contour, two traditional formulations are

widely used:

$$\nabla E_{ext}^1(x, y) = -|\nabla I(x, y)|^2 \quad (5)$$

$$\nabla E_{ext}^2(x, y) = -|\nabla(G_\sigma(x, y) * I(x, y))|^2 \quad (6)$$

Here,  $G_\sigma(x, y)$  is a two dimensional Gaussian function with standard deviation  $\sigma$  and  $\nabla$  is the gradient.  $I(x, y)$  represents the image intensity at a point  $(x, y)$ . In equation (6), the standard deviation is frequently used to control the capture range of the image features (in this case edges.) Setting higher values for  $\sigma$  is used to increase the capture range of the gradient forces, but it tends to blur and distort the edges [18]. An edge map can be defined as a bi-dimensional function  $f$  as follows:

$$f(x, y) = -E_{ext}^i(x, y) \quad (7)$$

for  $i = 1, 2$  (equations (5) and (6)).

In our work, we use  $E_{ext}^1$  as the external potential for all the calculations. Using this definition of an edge map the term  $\nabla f$  represents a field with vectors pointing toward the edges. The gradient vector flow is defined as a potential force with a vector field  $\mathbf{v}(x, y) = (u(x, y), v(x, y))$  that minimizes the energy functional:

$$\varepsilon = \int \mu(u_x^2 + u_y^2 + v_x^2 + v_y^2) + |\nabla f|^2 |\mathbf{v} - \nabla f|^2 dx dy \quad (8)$$

where  $\mu$  is a regularization parameter controlling the compromise between the first and second terms of the integral. This definition of  $\varepsilon$  guarantees that when  $\nabla f$  is near to zero (uniform regions), the second term will vanish and the field will be dominated by the squares of the partial derivatives of  $u$  and  $v$ , and it will vary in a very smooth way. If  $\nabla f$  has a high value, then the functional will be dominated by the second term and minimized when  $\nabla f \approx \mathbf{v}$ . In other words, this functional will have the effect of keeping  $\mathbf{v}$  nearly equal to the gradient of the edge maps when  $\nabla f$  is the most important component and varying in a smooth way in regular regions.

Using calculus of variations it is known [18] that the GVF field can be found by solving the following Euler equations:

$$\mu \nabla^2 u - (u - f_x)(f_x^2 + f_y^2) = 0 \quad (9a)$$

$$\mu \nabla^2 v - (v - f_y)(f_x^2 + f_y^2) = 0 \quad (9b)$$

where  $\nabla^2$  is the Laplacian operator. Equations (9a) and (9b) are known as the generalized diffusion equations. Note that in homogeneous regions, the second term of both equations is zero (because the gradient of  $f(x, y)$  is zero). These equations can be solved by treating  $u$  and  $v$  as functions of time and solving:

$$u_t(x, y, t) = \mu \nabla^2 u(x, y, t) - (u(x, y, t) - f_x(x, y)) \cdot (f_x(x, y)^2 + f_y(x, y)^2) \quad (10)$$

$$v_t(x, y, t) = \mu \nabla^2 v(x, y, t) - (v(x, y, t) - f_y(x, y)) \cdot (f_x(x, y)^2 + f_y(x, y)^2) \quad (11)$$

A stable finite difference implementation for solving the steady-state of these equations is given in detail in [17]. The calculated field  $\mathbf{v}$ , after the minimization process, replaces the potential force  $\nabla E_{ext}$  in equation (4). Figure 4(a) shows a CT image of an area around the right eye socket and in 4(b) its potential forces derived from the edges of the object (image features).

## 4 Including shape knowledge in the segmentation process

In our work, an additional term is included in the GVF snake formulation in order to incorporate knowledge about the shape to segment in a statistical way. The shape term is an adaptation of the one proposed by Cremers et al. [6, 7]. The central point of our proposal consists of combining image information and previously acquired shape information in a variational framework.

For a contour  $C = x(s)$  we will consider the following extended energy :

$$E = E_t + \gamma E_c(C) \quad (12)$$

where the term  $E_t$  is the energy contribution of a GVF active contour,  $E_c$  benefits contours with similar shapes to the one acquired in a shape training process, and  $\gamma$  is a factor to regulate the amount of influence of the shape term.

In general terms, the training process consists of collecting a set of similar shaped objects. We will adopt the concept of shape defined by Dryden [8], who defines the shape of an object as all the geometric features of the object that are unchanged

when it is translated, rescaled and rotated in an arbitrary coordinate system. In this work, the set of geometric features corresponds to a set of points placed along the object contour. The labelling of the control points can be done manually or automatically and the main objective is to create a reference set of control points to model the statistical shape variation.

The effect of combining  $E_t$  and  $E_c$  is twofold. First, it augments the capture range of potential field forces (which leads to less sensitivity to initialization). Second, it improves the capacity of the snake to deal with occlusion problems.

The following subsections describe the derivation of the  $E_c$  term of equation (12) which accounts for pre-established shape information.

### 4.1 Incorporating statistical shape information

In our work, the active contour  $C$  is represented with a quadratic B-spline curve given by [9]:

$$C : [0, 1] \rightarrow \Omega, \quad C(s) = \sum_{i=1}^n p_i B_i(s) \quad (13)$$

where  $s$  is the parameter of the spline,  $p_i$  is the set of control points, and  $B_i(s)$  are the quadratic periodic B-spline basis functions [9, 3].

A 2D object shape  $z$  is represented by a set of  $n$  pairs of control points  $\{(x_i, y_i)\}_{i=1 \dots n}$  defining the curve. The shape  $z$  can be referred to as a unidimensional vector with the following structure:

$$z = (x_1, y_1, \dots, x_n, y_n)^T \quad (14)$$

The main idea behind the shape formulation is the assumption that each trained shape will have the same number of related control points  $n$  and that the spatial position of each control point  $i$  can be modelled with a gaussian distribution. Figure 5 shows an example of this configuration for a four-shape training set. From this configuration we can obtain some parameters for the family of shapes as the mean shape  $\mu$  and the covariance  $\Sigma$  of the set.

The covariance matrix  $\Sigma$  defines a probability measure for the shape space. If the covariance matrix is full rank, its inverse  $\Sigma^{-1}$  exists and the Gaussian probability distribution of the shape  $z$  is :

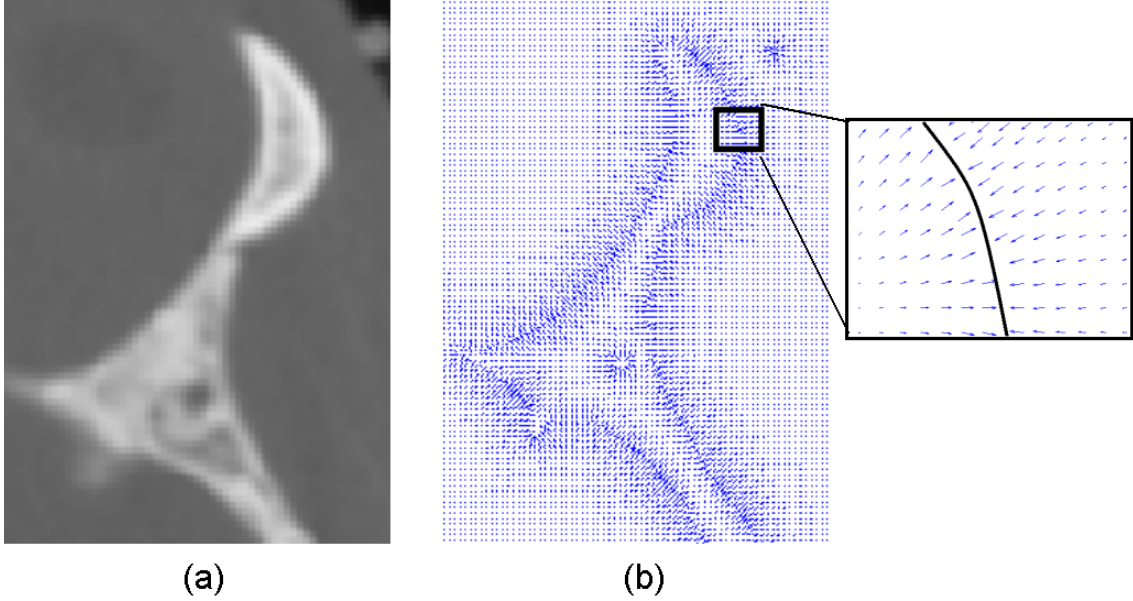


Figure 4: A portion of the skull around the right eye socket. (a) Original gray level CT image. (b) GVF field of the image and the rectangular marked area enlarged to the right. The black line represents a portion of the object boundary and the blue arrows the direction of the GVF potential forces.

$$\rho(z) \propto \exp\left(-\frac{1}{2}(z - \mu)^T \Sigma^{-1}(z - \mu)\right) \quad (15)$$

Here  $\propto$  denotes direct proportionality between the left and right expressions and  $\mu$  is the average shape of the training set. The requirement for  $\Sigma$  to be full rank is only accomplished by having at least  $2n$  different training shapes. In practical terms, this can be a strong limitation. To solve this problem, a technique of covariance regularization must be applied in order deal with a number of training shapes less than  $2n$ .

## 4.2 Regularizing the covariance

In general, regularizing a covariance matrix is not a trivial process. We follow the approach from [6] to propose an approximation to the solution. The covariance matrix can be expressed as a decomposition into eigenvalues and eigenvectors in the following way:  $\Sigma = VDVT^T$  where  $D$  is the diagonal matrix of non-zero eigenvalues  $\sigma_1 \geq \dots \geq \sigma_r > 0$ ,  $V$  is the matrix of corresponding eigenvectors and  $V^T$  is the transpose of  $V$ . The covariance matrix is

regularized by replacing all the zero eigenvalues by a constant  $\sigma_{\perp} > 0$ .

Thus, the new regularized covariance  $\Sigma_{\perp}$  is obtained by means of:

$$\Sigma_{\perp} = VD_{\perp}V^T \quad (16)$$

$$\text{with } D_{\perp} = D + \sigma_{\perp}(I - e_v e_v^T) \quad (17)$$

where  $e_v$  is an orthonormal basis of the matrix  $V$  of eigenvectors, and  $I$  is the identity matrix. For this work, as suggested in [6],  $\sigma_{\perp}$  is given by:

$$\sigma_{\perp} = \frac{\sigma_r}{2} \quad (18)$$

This expression guarantees that every possible variation in the shape space will have a corresponding value of probability  $\rho(z)$  covered by the new covariance matrix. Better yet, equation (15) will be differentiable on the full space, associating a finite non-zero value with any shape  $z$ . Equation (15) can be rewritten as:

$$\begin{aligned} \rho(z) &\propto \exp\left(-\frac{1}{2}(z - \mu)^T \Sigma^{-1}(z - \mu)\right) \approx \\ \rho(z) &= k \exp\left(-\frac{1}{2}(z - \mu)^T \Sigma^{-1}(z - \mu)\right) \end{aligned} \quad (19)$$

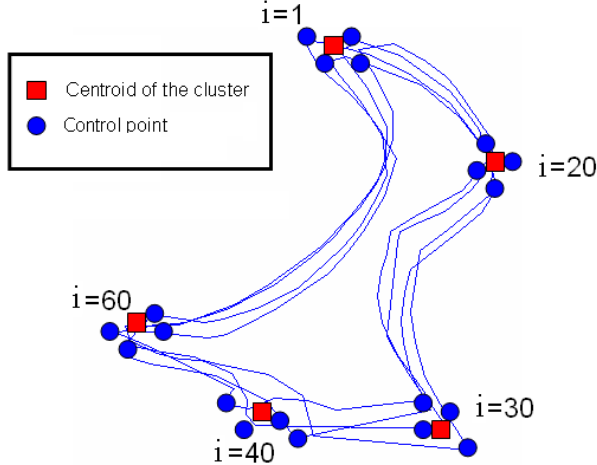


Figure 5: The figure shows control points  $i=1,20,30,40,60$  of four trained shapes and their related centroids. Each of the shapes is defined by 80 sampled points. The lines in blue show each shape trained after alignment.

for an arbitrary proportionality constant  $k$ . Applying the logarithm function to both sides of equation (19) and using the product rule for logarithms gives:

$$\log(\rho(z)) = \log(k) - \frac{1}{2}(z - \mu)^T \Sigma^{-1} (z - \mu) \quad (20)$$

Rearranging, equation (20) can be expressed in terms of a function of the shape  $z$  :

$$E_c(z) = \log(\rho(z)) + const = -\frac{1}{2}(z - \mu)^T \Sigma_{\perp}^{-1} (z - \mu) \quad (21)$$

with  $const = -\log(k)$ . With this algebraic development it is shown that the Gaussian probability in equation (15) corresponds to the quadratic energy in equation (21) [7].

### 4.3 Incorporating invariance in the shape term

So far, the term  $E_c$  in equation (12) is not invariant with respect to similarity transformations of the shape  $z$ . For an invariant scheme, the shape of the active contour  $z$  is first centered and then aligned

with respect to the regularised shapes of the training process. The term representing the centered shape version  $z_c$  can be obtained with :

$$z_c = (I_{2n} - \frac{1}{n}\Gamma) \cdot z \quad (22)$$

where  $I_{2n}$  denotes the identity matrix of size  $2n$ ,  $n$  is the number of control points and the  $2n \times 2n$  matrix  $\Gamma$  is given by:

$$\Gamma = \begin{pmatrix} 1 & 0 & 1 & 0 & \dots \\ 0 & 1 & 0 & 1 & \dots \\ 1 & 0 & 1 & 0 & \dots \\ \vdots & \vdots & \vdots & \vdots & \ddots \end{pmatrix} \quad (23)$$

The aligned shape vector  $\hat{z}$  is obtained by means of the following expression:

$$\hat{z} = \frac{Mz_c}{|Mz_c|} \quad (24)$$

with:

$$M = I_n \otimes \begin{pmatrix} \mu^T z_c & -\mu^T \times z_c \\ \mu^T \times z_c & \mu^T z_c \end{pmatrix} \quad (25)$$

where  $I_{2n}$  is the identity matrix with  $2n$  rows and the  $\otimes$  is the Kroenecker product. For more details of how to obtain these equations see [8] and [7]. The minimization of the shape functional  $E_c$  of the aligned and centered shape  $\hat{z}$  is obtained by deriving the shape term with respect to the shape  $z$  using the chain rule:

$$\frac{dE_c(\hat{z})}{dz} = \frac{dE_c(\hat{z})}{d\hat{z}} \cdot \frac{d\hat{z}}{dz} = \frac{dE_c(\hat{z})}{d\hat{z}} \cdot \frac{d\hat{z}}{dz_c} \cdot \frac{dz_c}{dz} \quad (26)$$

Each component is solved separately. From equation (21) and applying the product rule of a derivative:

$$\frac{dE_c(\hat{z})}{d\hat{z}} = (\Sigma_{\perp}^{-1}(z - \mu))^T \quad (27)$$

This term represents the gradient of the original shape energy  $E_c$  evaluated for the aligned shape  $\hat{z}$ .

From equation (22), deriving with respect to  $z$  :

$$\frac{dz_c}{dz} = (I_{2n} - \frac{1}{n}\Gamma) \quad (28)$$

This term reflects the change of the centered shape  $z_c$  with the the input shape  $z$ . The term  $\frac{d\hat{z}}{dz_c}$

accounts for the influence of changes in the centered shape  $z_c$  onto the aligned shape  $\hat{z}$ , and is expressed with the following equation:

$$\frac{d\hat{z}}{dz_c} = \frac{M'z_c + M}{\|Mz_c\|} - \frac{(Mz_c)(Mz_c)^T(M'z_c)}{\|Mz_c\|^3} \quad (29)$$

where  $M$  is the matrix defined in equation (25) and  $M'$  denotes the tensor of rank 3 given by:

$$M' = \frac{dM}{dz_c}$$

An algorithmic construction for  $M'$  and the detail of the derivation of this term can be consulted in [7].

## 5 Results

To test our algorithm, we have designed two groups of experiments: experiments with synthetic images and experiments with real images. The first group uses designed binary images which are synthetic images created with simple geometric objects. This design facilitates comparisons between the expected results and the outcomes of our segmentation approach. For the second category, the experiments were carried out with MR images from the VHP male dataset<sup>2</sup> [2, 13, 14]. These MR images were selected from areas of the head with different levels of difficulty in segmenting the skull. The training shape procedure is similar for both groups of experiments and will be described in the following subsection.

### 5.1 Training set creation

In all the experiments, the training set consists of six object shapes, which are in turn made up of a fixed number of sampled points taken along the object's perimeter at equal distances from each other. This number of control points is 40 for synthetic images and 80 for real images. Figure 6 shows an example of the training shapes acquired.

The trained shapes were acquired with a manual labelling process. The user is presented with an image containing one outline of one object. As

<sup>2</sup>Each of these is a gray-level image with a resolution of 256x256x16 bits.

the initial step, the user selects with the mouse a number of points on the object contour. The shape of the object is reconstructed from these points by means of a quadratic B-spline interpolation. The resulting curve is resampled and the control points are stored in the same order and number for each shape. This process is repeated six times for each object. The object outlines labelled were one ellipse and one rectangle for the experiment with synthetic images, and two anatomical contours for the experiment with real images. In the case of experiments with real images, since there is only one image for each anatomical region, the training process consists of manually labelling the skull area in the CT image (equivalent to the MR image to be segmented). Even though it seems like a lot of work for the synthetic images, the manual segmentation is useful to simulate the variation of the shape distribution. For real images there may be tens or hundreds of images to segment having similar shaped regions, and labelling just six is worthwhile if it gives better results for the rest of the images. Better yet, the results for the rest can then be fed back into the statistical model to improve it.

### 5.2 Synthetic images

For this group of experiments, two synthetic binary images were created. The object to segment in these images was represented as a closed region of pixels with constant intensity value of zero. The first image shown in figure 7(a) is an ellipse with outliers along its contour. The second image shown in figure 7(b) contains an object created with an ellipse and a rectangle superimposed to simulate an occlusion problem. Two experiments were designed in this group to show the functionality of the algorithm: one for segmenting a simple object in an image and one for segmenting different objects contained in the same image.

In the first experiment the objective was to show the capability of our algorithm to recover the underlying elliptic shape of the image in figure 7(a). This problem can be considered similar to the one of eliminating the 'outliers' of the elliptic shape. The results of this experiment for two sets of parameters are shown in figure 8.

In figure 8, each row represents the result of the algorithm for different  $\gamma$  values.



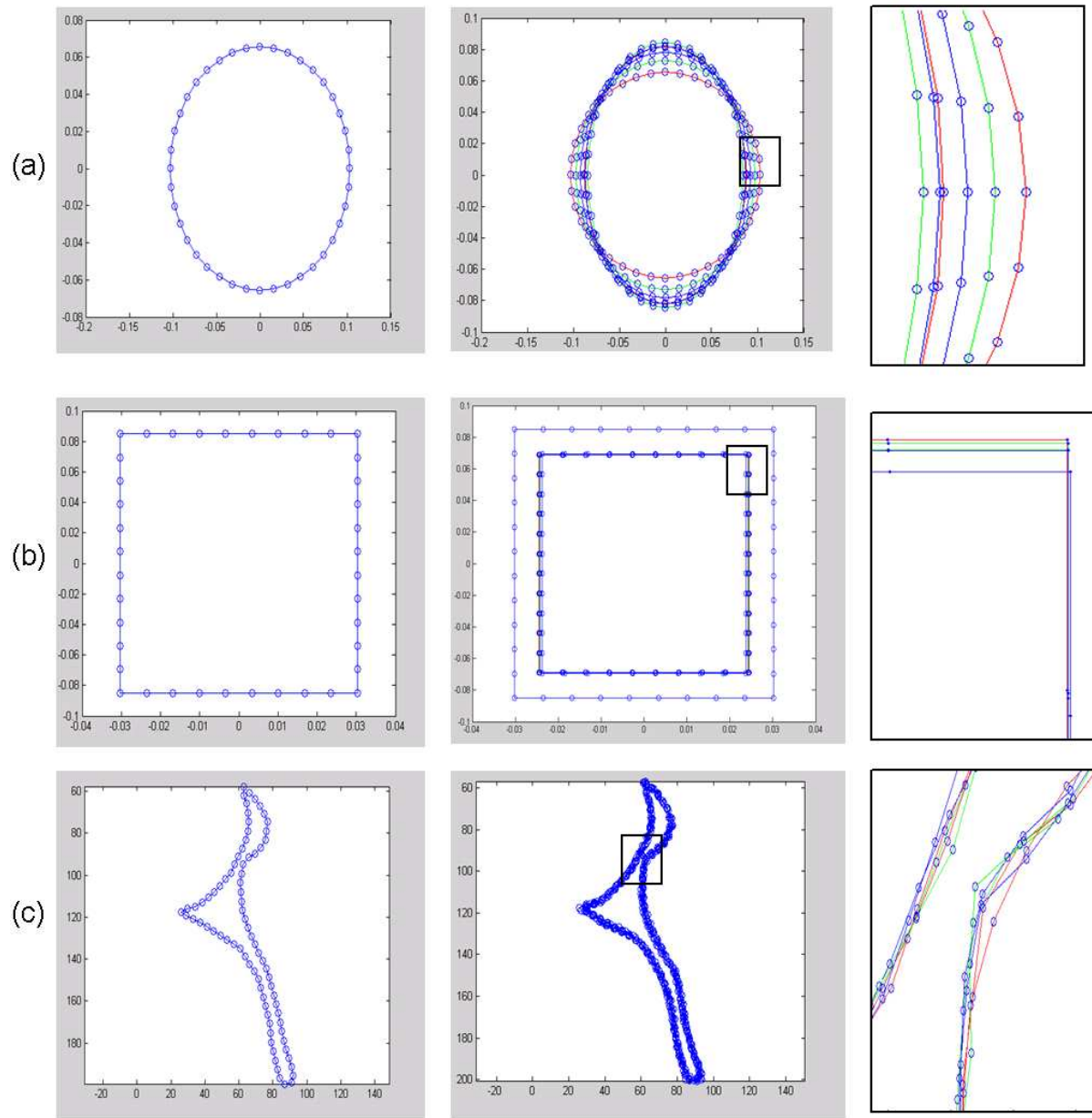


Figure 6: Examples of one element of each training set.(a) Ellipse with 40 control points. (b)Rectangle with 40 control points and (c) A portion of the skull represented with 80 control points. The first column shows one element of each training set. The second column shows the six shapes acquired for each object, and the third column shows a detail of the distribution of the control points in the squared area marked in the image of the second column.

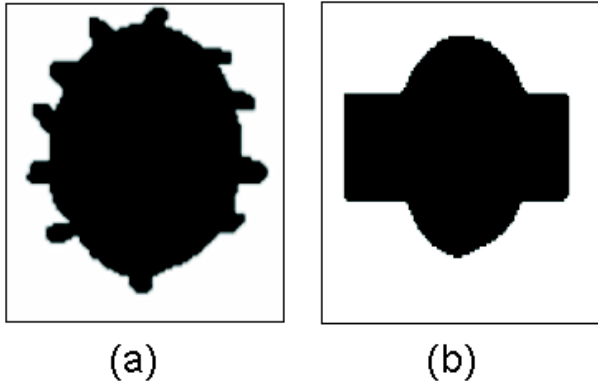


Figure 7: Two synthetic images created for segmenting simple objects.

For the first row, with  $\gamma = 0$  (no shape component considered), we would expect a segmentation driven by the image features, with the resulting contour and the feature map being approximately the same. The result in the right column of the first row corroborates our expectations.

The second row shows that it is possible to extract an approximation of the underlying ellipse according to the image features present and the statistics contained in the training shape set. Here, a value of  $\gamma = 100$  was used to incorporate the shape component in the segmentation process.

With these two results, it can be shown that, depending on the specific requirements, we can control the behaviour of the algorithm with the shape parameters.

The second experiment consists of two stages. In the first stage, an elliptic shape object will be recovered from the image in figure 7(b). In the second stage, the rectangular object will be extracted. The aim of this experiment was to demonstrate the capability of our algorithm to include statistical shape knowledge for different trained shapes as well as to demonstrate how the shape parameter affects the results for different values.

Figure 9 presents three results of our algorithm applied to the image in figure 7(b). As in figure 8 each row represents the outcomes of the algorithm for different  $\gamma$  values. The parameter combination is presented in table 1. As expected, setting  $\gamma = 0$  results in the whole contour of the composed object being detected. For  $\gamma = 20$ , an acceptable approximation to the elliptic shape is obtained, even

though the final shape is not as smooth as a ‘perfect’ ellipse. For  $\gamma = 200$ , the resulting shape is almost a ‘perfect’ smooth ellipse at the cost of less fidelity to the image features, as shown in the second column of the third row.

Row #	Shape term	Tension, Rigidity and influence	Trained shape
1	$\gamma = 0$	$\alpha = \beta = \mu = 0.5$	Ellipse
2	$\gamma = 20$	$\alpha = \beta = \mu = 0.5$	Ellipse
3	$\gamma = 200$	$\alpha = \beta = \mu = 0.5$	Ellipse

Table 1: Parameters for segmenting the image in figure 7(b) using an elliptic trained shape.

Figure 10 shows the results for the second stage of this experiment which considers a rectangular training shape. In this case similar results to the ellipse segmentation were obtained. The first row shows the whole contour coinciding with the final snake. The second row shows a contour ‘trapped’ between the forces of the GVF potential and the shape potential. In this case, the contour converges to a bad solution with just some portion of the rectangular shape detected. In the third row, the shape term of the snake is high enough to deform the active contour towards the borders of the rectangular contour. Finally, the last row shows an almost rectangular shaped result. It is important to bear in mind that the rounded corners of the ‘rectangular’ shape are due to the small quantity of sampled points and the interpolation used to represent the shape models, and this effect can be reduced by increasing the number of control points and modifying the restriction of the uniform distribution of the control points.

Row #	Shape term	Tension Rigidity	Trained shape
1	$\gamma = 0$	$\alpha = \beta = \mu = 0.5$	Rectangle
2	$\gamma = 10$	$\alpha = \beta = \mu = 0.5$	Rectangle
3	$\gamma = 80$	$\alpha = \beta = \mu = 0.5$	Rectangle
4	$\gamma = 100$	$\alpha = \beta = \mu = 0.5$	Rectangle

Table 2: Parameters for segmenting the image in figure 7(b) using a rectangular trained shape.

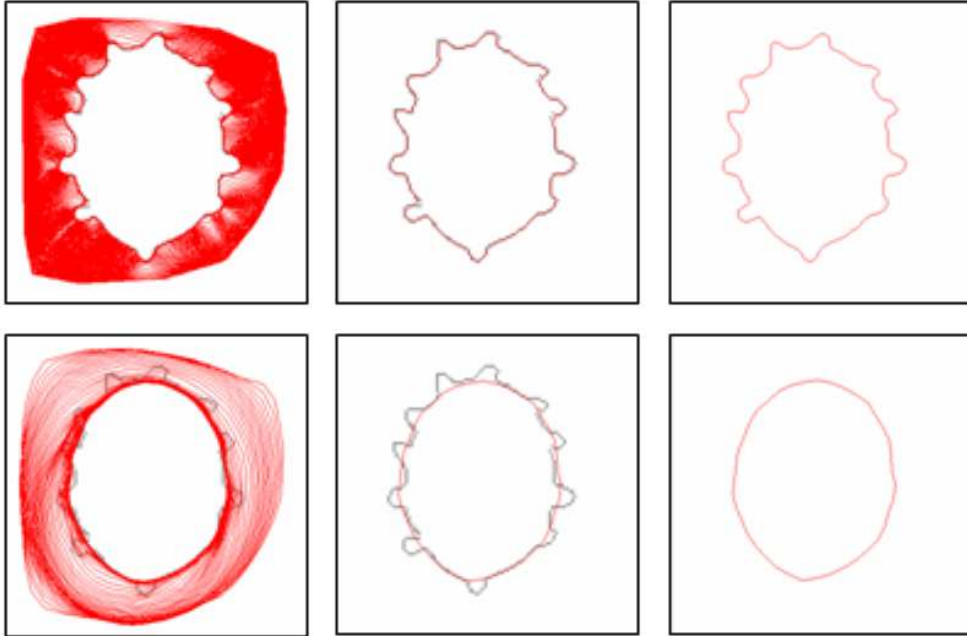


Figure 8: Two results of segmenting the image in figure 7(a). The parameters used in the first row are  $\gamma = 0$ ,  $\alpha = \beta = 0.5$  and the parameters used in the second row are  $\gamma = 100$ ,  $\alpha = \beta = 0.5$ . The first column displays the active contour evolution at each iteration (red lines) overlaid on the feature map (gray pixels). The evolution of the active contour illustrates the action of the GVF field in attracting the snake towards the feature map. The central column shows a comparison between the final state of the snake and the feature map (gray line). The rightmost column of this figure displays the resulting detected contour.

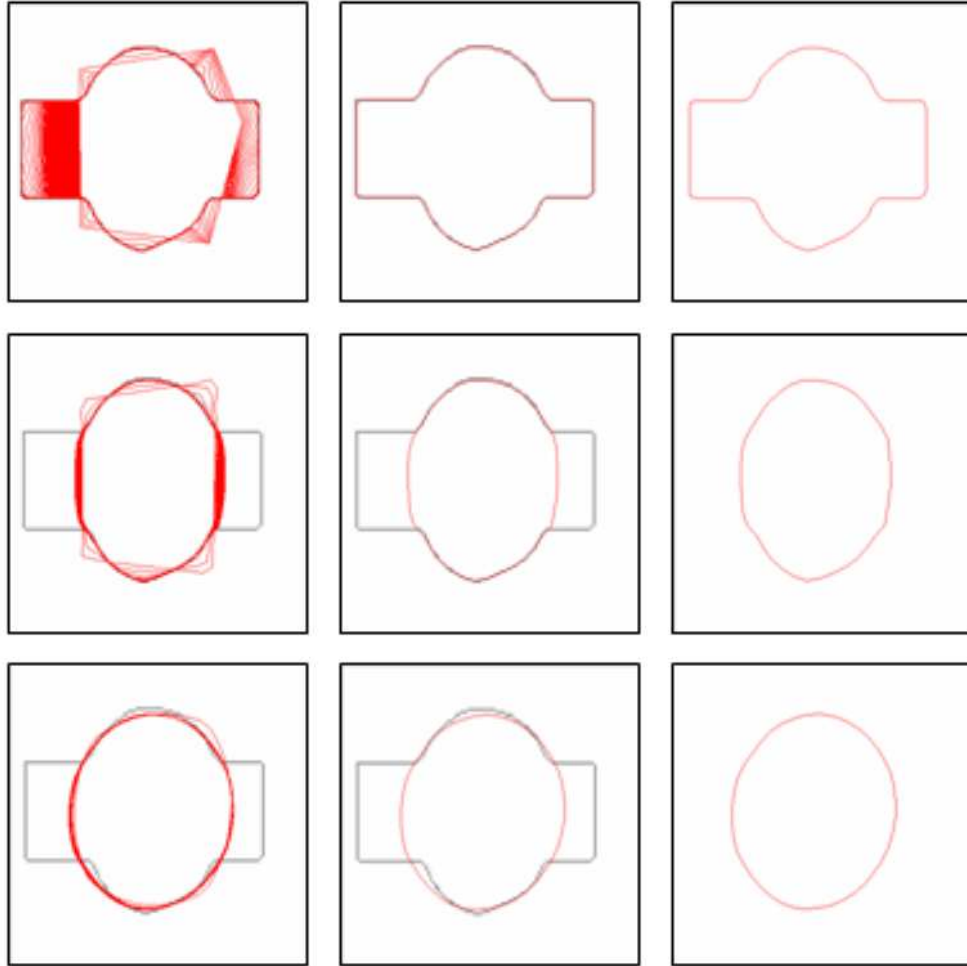


Figure 9: Extracting an elliptic shape from image in figure 7(b). Table 1 gives the parameters used for each row. The first column displays the active contour evolution at each iteration (red lines) overlaid on the feature map (gray pixels). The central column shows a comparison between the final state of the snake and the feature map (gray line). The rightmost column of this figure displays the resulting detected contour.

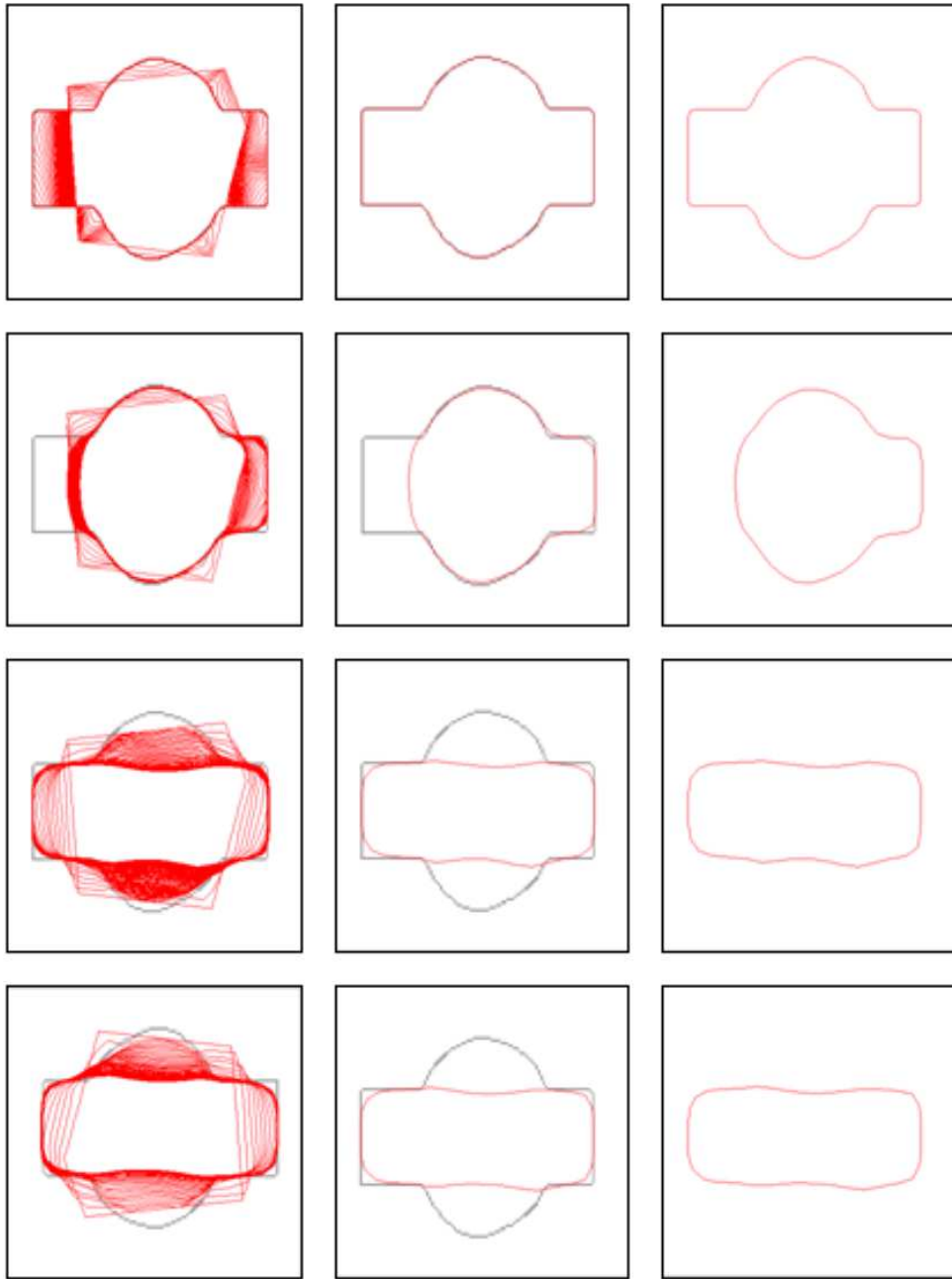


Figure 10: Extracting a rectangular shape from the image in figure 7(b). Table 2 gives the parameters used for each row. The first column displays the active contour evolution at each iteration (red lines) overlaid on the feature map (gray pixels). The central column shows a comparison between the final state of the snake and the feature map (gray line). The rightmost column of this figure displays the resulting detected contour.

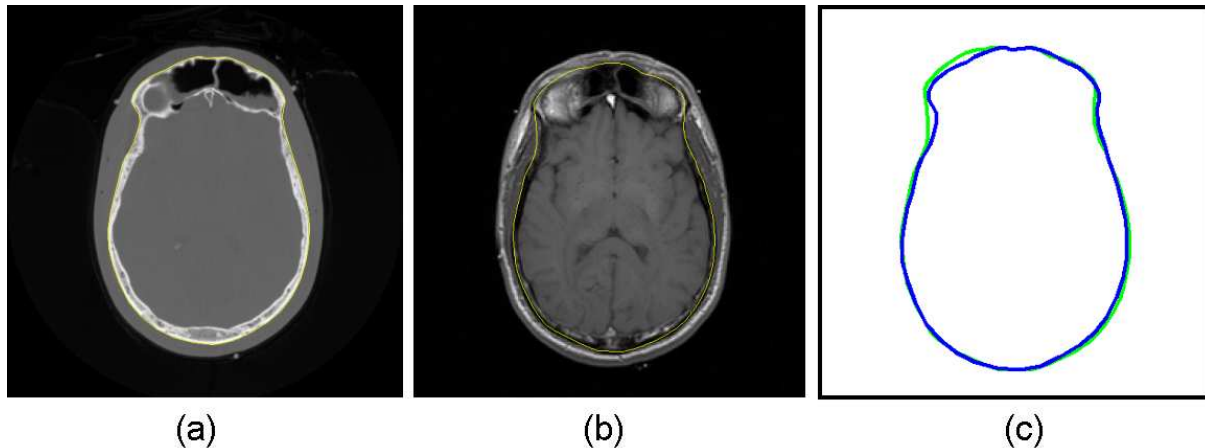


Figure 11: Segmenting an MR image with homogeneous pixel intensities for the bone regions. (a) The CT image showing clearly the area to be considered as bone for this slice level. (b) The MR image to segment. The yellow line represents the resulting active contour. (c) A comparison between the CT (blue) and the MR (green) segmentation.

### 5.3 Real images

In this category of experiments the objective was to segment a portion of the skull in a gray-level MR image. Two experiments were conducted for two different areas of the head. These areas were chosen in order to illustrate the functionality of our algorithm under extreme conditions: an easy area containing an homogeneous bone region and a more complicated region where the skull intensities are not completely homogeneous. The CT versions of the same areas of the MR images are available and are used for evaluating the results of the MR segmentation. In both experiments the values for  $\alpha$ ,  $\beta$  and  $\mu$  were fixed to 0.5, and the threshold was fixed to  $0.3I_{\max}$  (where  $I_{\max}$  = maximum intensity of the image).

The first experiment consists of segmenting the area of the head shown in figure 11. The figure shows the MR image to segment as well as the reference CT scan used to train the shape and evaluate the results. The area of the head in the images is a region slightly above the eye cavities with a view from above the head. As in the case of the synthetic images, the procedure described in section 5.1 was used to create the training set. In our proposed approach, if parameter  $\gamma$  is set to zero the segmentation process will be governed just for the image features present in the image which leads to

a pure data driven segmentation. In this case, only the dark areas of the image in fig. 11(b) are taken into account.

The result of the MR segmentation is shown with a green line in figure 11(c). For this area, given the smooth variation of the skull and the homogeneity of its defining pixels in the MR image, we expect to get good results by neglecting the shape term in our algorithm. The comparison between the MR segmentation (green line) and the CT segmentation (blue line) shown in fig. 11(c) presents evidence of this. The average error between the correct segmentation and the final active contour obtained from the MR segmentation is  $\bar{e} = 1.97$  pixels with a standard deviation  $\sigma = 0.87$  pixels. This error rate is calculated by averaging the distances between the control points from the CT segmentation and the control points from the resulting MR segmentation and assuming that the CT segmentation represents the correct shape at the correct position.

The second experiment of this group consists of segmenting the bone area shown in figure 12 including shape information. This area corresponds to a portion of the MR image shown in figure 2 selected around the right eye cavity. Figure 12(a) shows the CT gray-level image of this region and figure 12(b) shows the MR image of the same region of the head.

The objective of this experiment was to illustrate the difference between a “blind” segmentation method and one using knowledge about the shape to be segmented. The selected region contains a skull area difficult to segment given the pixel intensity variations of the bone regions.

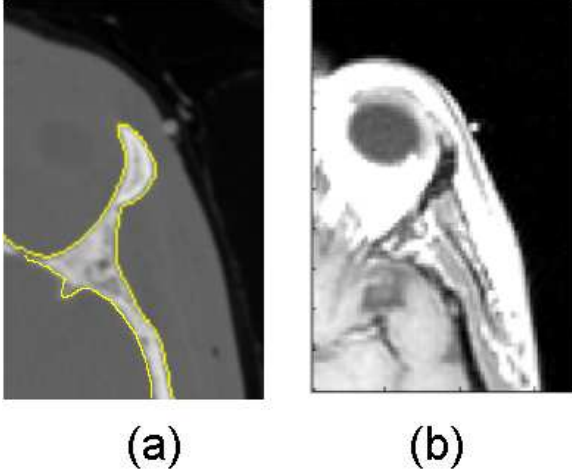


Figure 12: Area of the head around the right eye cavity. (a) A portion of the CT scan. The yellow line shows the contour used as a reference for the labelling task in the training process. (b) The same region scanned with a MR scan.

Figure 13 displays some results for different  $\gamma$  values. If the  $\gamma$  value is increased, the shape information influences the outcome resulting in a scheme directed by the shape. This will compensate for the missing information of bone components of high intensity in the MR image. A very high value of  $\gamma$  will conduct the resulting segmentation to a shape configuration within the distribution of the trained shapes.

As can be seen in figure 14(a) the result of a pure feature driven segmentation in this area gives a poor segmentation of the expected shape because of the variability of pixel intensities in bone regions. This figure shows with a yellow line the final contour obtained when no shape information is added.

Figure 14(b) shows the result (with a black line) of incorporating a high shape component by setting a threshold value of 0.3 and  $\gamma = 4.0 \times 10^7$ . This figure shows the final state of the snake after 40 iterations.

Figure 14(c) shows a comparison between a CT

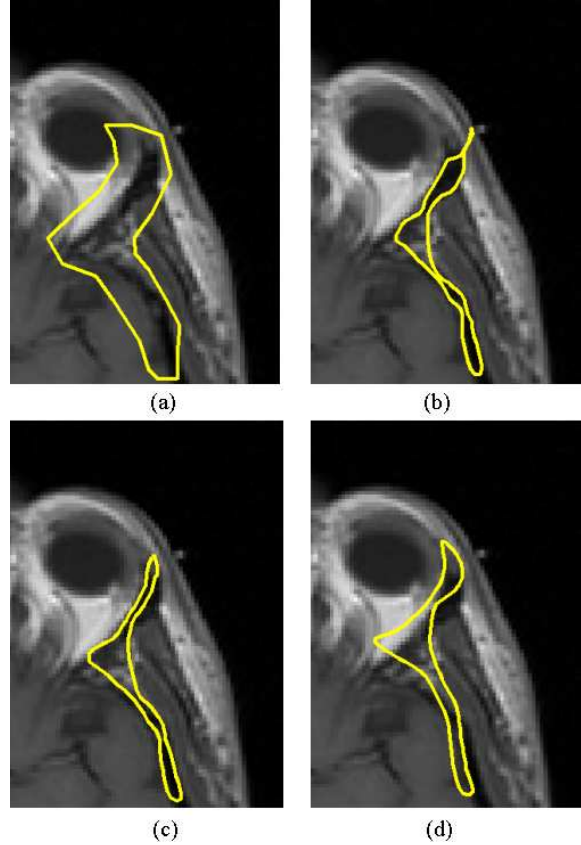


Figure 13: Results of the MR segmentation for different shape parameters. (a) Initialization. Result for: (b)  $\gamma = 1 \times 10^7$  (c)  $\gamma = 2 \times 10^7$  and (d)  $\gamma = 5 \times 10^7$

image segmentation and the result of segmenting the MR image of 12(b) with the shape component included. The resulting shape (green line) is very close in dimensions to the desired ideal segmentation (blue line) for these parameters. The resulting contour presents an average error  $\bar{e} = 10.75$  pixels and a standard deviation of  $\sigma = 6.3$  pixels. This error rate is calculated in the same way as in the previous experiment.

## 6 Conclusions

This work has presented a gradient vector flow (GVF) snake extended to include statistical shape information. The algorithm proposed can be used



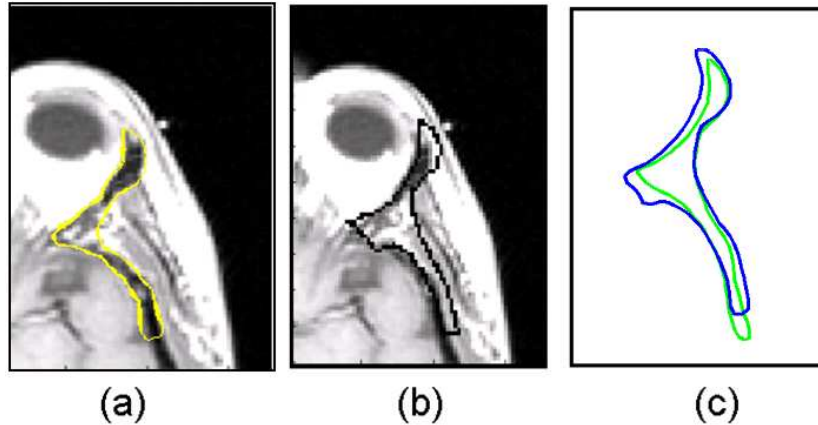


Figure 14: Results of segmenting the area shown in figure 12. (a) Pure feature driven segmentation. The yellow line shows the final contour after 100 iterations (no shape information included). (b) Segmenting including a shape component. Here, the black line shows the final result. (c) Comparison between a CT segmentation (blue line) and the MR segmentation of the same area of the head (green line).

to deal with problems of outliers and occlusion. Its application was tested for segmenting bone areas in MR images. The experiments reported in this document show that it is possible to create approximations to the external surface of the skull in a continuous way and with low error rates. In general the behaviour of the algorithm can be controlled by tuning some of the parameters. The strength of the shape force has to be adjusted for each dataset because of the requirements that it must be large enough to overcome weak edges and noise, but small enough so it doesn't overwhelm legitimate edge forces.

The current approach can be used to remove outliers and noise in areas with smooth shape variations. Given the properties of the skull, some areas appear partially defined in the MR scan images. Our method can be trained to compensate for information about the skull regions that could be difficult to separate in an MR image, exploit the information present and estimate the missing parts. This method was implemented in 2D. However it could be extended to 3D to segment the complete skull by treating the set of MR scans as a volume rather than separate scans.

To improve the algorithm, the deformation at a given contour level in the skull dataset could be restricted by taking into account the skull shape variation with respect to the previous contour level.

Furthermore, the current proposal could be extended to incorporate knowledge about an approximated skull shape variation obtained from the associated face layer (which is easily extractable from the MR datasets).

M.S. acknowledges CONACyT-Mexico for the scholarship support.

## References

- [1] R. Acharya and R.P. Menon. A review of medical image segmentation techniques. In Computer Society Press, editor, *Deformable models in medical image analysis*, pages 140–161. IEEE, 1998.
- [2] M.J. Ackerman. The Visible Hman Project. *Proc. I.E.E.E.*, 86(3):504–511, 1998.
- [3] A. Blake and M. Isard. *Active Contours*. Springer, London, 1998.
- [4] V. Caselles, F. Catte, T. Coll, and F. Dibos. A geometric model for active contours. *Numerische Mathematik*, 66:1–31, 1993.
- [5] V. Caselles, R. Kimmel, and G. Sapiro. Geodesic Active Contours. *International Journal of Computer Vision*, 22(1):61–79, 1997.



- [6] D. Cremers, C. Schnorr, J. Weickert, and C. Schellewald. Diffusion-Snakes Using Statistical Shape Knowledge. In *Lecture Notes in Computer Science*, volume 1888, pages 164–174, 2000.
- [7] D. Cremers, F. Tschhäuser, J. Weickert, and C. Schnorr. Diffusion-Snakes: Introducing Statistical Shape Knowledge into the Mumford-shah functional. In *International Journal of Computer Vision*, volume 50, pages 295–313, 2002.
- [8] I.L. Dryden and K.V. Mardia. *Statistical Shape Analysis*. John Wiley, 1st? edition, July 1998.
- [9] G. Farin. *Curves and Surfaces for Computer-Aided Geometric Design*. Academic Press, San Diego, 1997.
- [10] K. Han Horst and Heinz-Otto Peitgen. The Skull Stripping Problem in MRI Solved by a Single 3D Watershed Transform. In *Proceedings of MICCAI*, pages 134–143. Lecture Notes in Computer Science, October 2000.
- [11] M. Kass, A. Witkin, and D. Terzopoulos. Snakes: Active contour methods. *International Journal of Computer Vision*, pages 312–333, 1998.
- [12] R. Malladi, J. A. Sethian, and B.C. Vemuri. Shape modeling with front propagation: A level set approach. *IEEE Transactions on Pattern Analysis and Machine Intelligence*, 17(2):158–175, 1995.
- [13] National Library of Medicine. Visible Human Project, 1986. <http://www.nlm.nih.gov/research/visible/>; last accessed June 2007.
- [14] V. Spitzer, M.J. Ackerman, A.L. Scherzinger, and D. Whitlock. The Visible Human Male: A Technical Report. *JAMIA*, 3(2):118–130, 1996.
- [15] D. Terzopoulos, A. Witkin, and M. Kass. Constraints on deformable models: Recovering 3d shape and nonrigid motion. *Artificial Intelligence*, 36(1):91–123, 1988.
- [16] D. Vandermeulen, P. Claes, and P. Suetens. Volumetric Deformable Face Models for Cranio-facial Reconstructions. *Proceedings of the 4th Symposium on Image and Signal Processing Analysis*, pages 353–358, 2005.
- [17] C. Xu and J. L. Prince. Snakes, shapes, and gradient vector flow. Technical report, The Johns Hopkins University, October 1996.
- [18] C. Xu and J. L. Prince. Gradient Vector Flow: A New External Force for Snakes. *IEEE Proceedings Conference on Computer Vision and Pattern Recognition*, pages 66–71, 1997.